



Numerical investigation of interfacial transport resistance due to water droplets in proton exchange membrane fuel cell air channels



Mustafa Koz^a, Satish G. Kandlikar^{a,b,*}

^a Microsystems Engineering, Rochester Institute of Technology, 168 Lomb Memorial Dr., Rochester, NY 14623, USA

^b Mechanical Engineering, Rochester Institute of Technology, 76 Lomb Memorial Dr., Rochester, NY 14623, USA

H I G H L I G H T S

- Interfacial oxygen resistance in an air channel is numerically calculated.
- The effect of liquid water droplets on the resistance is investigated.
- The resistance is shown to decrease with air velocity, droplet size, and number of droplets.
- Spacing between the droplets is studied for the lowest resistance.
- The analogy between heat and mass transfer is investigated for this problem.

A R T I C L E I N F O

Article history:

Received 19 February 2013

Received in revised form

14 May 2013

Accepted 13 June 2013

Available online 21 June 2013

Keywords:

PEM fuel cell

Interfacial transport

Droplet

Simulation

Sherwood number

Nusselt number

A B S T R A C T

Oxygen transport resistance at the air flow channel and gas diffusion layer (GDL) interface is needed in modelling the performance of a proton exchange membrane fuel cell (PEMFC). This resistance is expressed through the non-dimensional Sherwood number (Sh). The effect of the presence of a droplet on Sh is studied numerically in an isolated air flow channel using a commercially available package, COMSOL Multiphysics®. A droplet is represented as a solid obstruction placed on the GDL–channel interface and centred along the channel width. The effect of a single droplet is first studied for a range of superficial mean air velocities and droplet sizes. Secondly, the effect of droplet spacing on Sh is studied through simulations of two consecutive droplets. Lastly, multiple droplets in a row are studied as a more representative case of a PEMFC air flow channel. The results show that the droplets significantly increase Sh above the fully developed value in the wake region. This enhancement increases with the number of droplets, droplet size, and superficial mean air velocity. Moreover, the analogy between mass and heat transfer is investigated by comparing Sh to the equivalent Nusselt number.

© 2013 Elsevier B.V. All rights reserved.

1. Introduction

The performance loss due to oxygen (O_2) transport resistance on the cathode side of a proton exchange membrane fuel cell (PEMFC) is an active area of research. The O_2 transport loss becomes more significant as the current density increases. The increased transport resistance is partly due to the increased water production rate at higher current densities. The O_2 transport resistance has a non-negligible component at the gas diffusion layer (GDL)–air flow channel (Ch) interface. It has not yet been shown how water droplets on the GDL–Ch interface affect the transport resistance.

The interfacial O_2 transport resistance can be used in simplified PEMFC performance models [1–4]. This resistance is expressed through the non-dimensional Sherwood number (Sh), which is the mass transfer equivalent of the Nusselt number (Nu) for heat transfer. For fully developed flow conditions (FD), using the heat and mass transfer analogy, Sh can be taken directly from the established values of Nu for a variety of channel cross sections and boundary conditions. It is important to match the equivalent boundary condition in the associated heat and mass transfer problems with fully developed conditions. However, the flow in a PEMFC air channel may not be fully developed for two reasons: 1) suction or injection of air at the porous GDL–Ch interface, and 2) water features disrupting the air flow in the channel.

The effect of suction/injection has been studied numerically in 2D air channels (parallel plates) [5–7]. Wang et al. simulated the cathode half of a PEMFC and reported that the suction/injection did

* Corresponding author. Mechanical Engineering, Rochester Institute of Technology, 76 Lomb Memorial Dr., Rochester, NY 14623, USA. Tel.: +1 585 475 6728; fax: +1 585 475 6879.

E-mail addresses: mxk7984@rit.edu (M. Koz), sgkeme@rit.edu (S.G. Kandlikar).

Nomenclature*Abbreviations*

Ch	air channel
CL	catalyst layer
FD	fully developed
GDL	gas diffusion layer
PEMFC	proton exchange membrane fuel cell

Variables

Bo	bond number
C	oxygen molar concentration
C_p	constant pressure heat capacity of air
d_h	hydraulic diameter
D_{O_2-air}	molar oxygen diffusivity in air
D_{O_2-GDL}	molar oxygen diffusivity in the gas diffusion layer
F	air drag force on a droplet
F_c	Faraday's constant
g	gravitational acceleration
h	convective transport coefficient
H	air channel height
i	current density
I	identity matrix
j	molar flux of oxygen
k	thermal conductivity of air
L	simulated air channel length
N	droplet number in the air flow direction
Nu	Nusselt number
p	air pressure
Po	Poiseuille number
q''	heat flux
r	droplet obstruction radius
R_u	universal gas constant
Sh	Sherwood number
t	gas diffusion layer thickness

T	temperature
u	velocity vector
u, v, w	velocity components
W	air channel width
We	Weber number
x	spatial coordinate vector
x, y, z	spatial coordinate components
Δx	distance in the flow direction

Greek

ε	thermal conductivity or species diffusivity
μ	dynamic viscosity of air
Ω	Nusselt or Sherwood number
ρ	air mass density
ψ	thermal or mass convective transport coefficient
$\bar{\psi}$	channel width averaged ψ
σ	air–water surface tension
θ	droplet static contact angle
ξ	channel cross sectional area blockage ratio by droplet

Subscript

av	flow direction averaged
d	droplet
eff	effective
FD	fully developed
m	mean
M	mass transport related
max	the maximum value from the wake of the droplet of interest
N	droplet number in the flow direction
T	thermal transport related
x	flow direction specific
wet	portion of GDL–Ch interface covered by droplet

Superscript

T	transpose
---	-----------

not change Sh relative to the case with no suction/injection [5]. Jeng et al. [6] also simulated the cathode side of a PEMFC and confirmed the negligible effect of air injection into the channel on Sh reported by Wang et al. [5]. Hassanzadeh et al. [7] simulated an isolated reactant channel along with the boundary conditions to mimic PEMFC conditions. They parametrically investigated the effect of air suction into the GDL. A weak dependency of Sh was found on the suction rate. In summary, the 2D numerical studies suggest that the intensity of suction/injection in a PEMFC operation leads to a minor change in Sh.

In order to study the effect of liquid water features on Sh, visual characterization of the water features is required. After characterizing the shapes, sizes, and motion of the water features, these features can be incorporated into simplified models as obstructions to single-phase flow without the need for simulating the complex two-phase flow. The liquid water present in the reactant channels can be characterized through visible-light-transparent PEMFC designs. The use of visible light provides high spatial and temporal resolution compared to other options, such as X-ray radiography, neutron radiography, and magnetic resonance imaging [8]. The two-phase flow in channels of an operational PEMFC was visualized by in-situ studies [2,8–17]. Numerical investigations aim to explain the experimentally visualized trends by parametrically analyzing the two-phase flow in 3D channels [11,19–28]. Some of the numerical studies complement their research with ex-situ experiments that introduce the liquid water into PEMFC channels through

artificial injection [11,19,21,28]. Moreover, there are dedicated ex-situ studies that focus on liquid droplet dynamics [29–35]. Since liquid water comes out of the GDL in the form of a droplet first and then evolves into more complex shapes such as films and slugs (also known as plugs), this study focuses on the effect of droplets on Sh.

The Sherwood number is obtained by non-dimensionalizing the mass transfer coefficient (h_M) with diffusivity (D) and channel hydraulic diameter (d_h): $Sh = h_M d_h / D$. The Sherwood number reported by Wang et al. was obtained using the channel height for two parallel plates as the characteristic length instead of the hydraulic diameter [5]. The Sherwood number calculated by Wang et al. [5] is reported here with the standard definition by using the fact that the hydraulic diameter for parallel plates is two times the channel height. Wang et al. [5], Jeng et al. [6], and Hassanzadeh et al. [7] numerically calculated Sh_{FD} as 5.274, 6.0, and 5.411, respectively, in 2D simulations. The effect of a water droplet emerging from the GDL–Ch interface on Sh was first investigated by Koz and Kandlikar [36]. For a 3D rectangular channel with a width and height of 0.70 mm and 0.40 mm respectively, they numerically calculated $Sh_{FD} = 3.36$, which is significantly lower than the reported 2D values. Simulations incorporated a water droplet on the GDL–Ch interface in the form of a droplet-shaped solid obstruction centred along the channel width. The droplet adhesion to the GDL–Ch interface was assessed by comparing the numerically calculated drag force on the obstruction against the

experimentally obtained force to initiate droplet sliding [34]. They found that Sh was increased with respect to the fully developed value, Sh_{FD} , downstream of the water droplet.

As a follow up to the reported efforts on Sh affected by a water droplet [36], this numerical study aims to show the effects of single and multiple droplets on Sh . Initially, it was assessed whether a droplet at a given superficial mean air velocity and droplet size can remain adhered to the GDL–Ch interface and retain its spherical shape. This assessment was conducted for all possible sets of droplet size and air velocity values which were taken from the initially proposed parametric ranges. As a result, possible sets of the aforementioned parameters were obtained to simulate cases with droplet adhesion and spherical shapes. By using these possible sets of parameters, the effect of droplet size and air velocity on Sh for a single droplet was studied. The effect of droplet spacing on Sh is shown for two consecutive droplets. The effect of multiple droplets in a row on Sh is shown by eleven uniformly spaced droplets. Moreover, the heat and mass transfer analogy was investigated in the same geometry by separately solving the equivalent heat and mass transfer problems. The numerically calculated results of Sh and Nu are compared in the channel for fully developed flow as well as the flow behind the droplets, and local variations of Sh and Nu are reported. The numerically calculated Nu values can be a validation ground since the equivalent heat transfer problem may be experimentally investigated more easily than the mass transfer problem.

2. Methodology

2.1. Introduction to the problem geometry and physics

A single PEMFC air flow channel was isolated from the neighbouring ones. The active area under a repeating pattern of a channel and a land (area between two channels) was used to calculate the superficial mean air velocity in the channel. Fig. 1 shows the channel width (W), height (H) and the simulated length (L), which was taken as 83.00 mm and is shorter than the total active area length. The active area width and length, and the channel width (W) and height (H), are 1.20 mm and 183.00 mm, 0.70 mm, and 0.40 mm, respectively. These dimensions were taken from the parallel channel design that meets the performance targets by the United States Department of Energy [37]. The corresponding hydraulic diameter (d_h) is 0.51 mm.

Fig. 1a shows multiple droplet-shaped obstructions in the air flow channel. These obstructions are hollow, and only their boundaries were utilized to obstruct the flow. Each droplet is numbered consecutively in the flow direction (N). The coordinates of each droplet ($x_{d,N}$) differ in the flow direction ($x_{d,N}$) while all droplets were placed on the GDL–FF interface ($z_{d,N} = 0$) and

centred along the channel width ($y_{d,N} = W/2$). Although droplets can emerge from random positions on the GDL, centering the droplet along the channel width is a reasonable assumption since in-situ visualization studies [9–11,14,18] showed droplets positioned on the interface with a slight offset from the channel width centre. The first droplet was positioned at 63.00 mm from the inlet to eliminate the entrance region effect. When there was more than one droplet, the uniform distance between any two consecutive droplets (Δx_d) was measured between the droplet centres.

A droplet-shaped solid obstruction was created with a sphere that had radius (r). In order to mimic the hydrophobic nature of the GDL, the static contact angle (θ) was taken as 147° , which is a representative value for a typical GDL used in experiments [32,34]. Fig. 1b shows the droplet obstruction partially covering ($W_{wet}(x)$) the GDL–Ch interface.

Air properties were assumed to be constant and uniform throughout the channel at a temperature (T) of 80°C and 100% relative humidity. Mass density (ρ), dynamic viscosity (μ), thermal conductivity (k), and heat capacity (C_p) were calculated with the correlations provided by Tsilingiris [38]. Oxygen diffusivity in the air ($D_{O_2-\text{air}}$) was approximated by Wilke's formula [39] incorporating the vapour saturation pressure correlation [40] and the diffusivity correlation for air components [41]. With the aforementioned air properties, the Prandtl ($Pr = C_p\mu/k$) and Schmidt ($Sc = \mu/(\rho D_{O_2-\text{air}})$) numbers were calculated. The air properties used in this study are summarized in Table 1.

The superficial mean air velocities (u_m) were calculated based on the current density (i) and the associated stoichiometry. For most cases the air flow rate was simulated with a stoichiometry of 2, except for $i = 0.1 \text{ A cm}^{-2}$, for which a stoichiometry of 3 was used. The corresponding air velocity range for $i = 0.1\text{--}1.5 \text{ A cm}^{-2}$ was calculated as $u_m = 1.59\text{--}15.89 \text{ m s}^{-1}$. Mapping i to u_m was performed only to roughly predict what the u_m range can be for a channel during cell operation. The mapping above represents the case that the air flow on the cathode side is evenly distributed to the parallel air channels through the manifold. Experiments by Lu et al. [42] showed that there can be a flow maldistribution among the air channels due to varying two-phase flow resistance in each channel. In order to predict the Sherwood number for a given instant and channel, simulations should be conducted for a wide range of u_m that accounts for all possible outcomes of flow maldistribution. The u_m range selected here is wide enough for the following two reasons: 1) as to be discussed in Section 5.3, the lowest u_m will lead to a very insignificant boundary layer separation in the wake of a droplet. Hence, any velocity smaller than 1.59 m s^{-1} would lead to a very similar result to $u_m = 1.59 \text{ m s}^{-1}$. 2) As to be shown in Section 2.2, the highest u_m in the selected range prevents all droplet sizes except one to adhere to the GDL–Ch interface and remain close to a spherical shape. Any u_m larger than the already selected maximum u_m would not allow the smallest droplet size to adhere to the interface and remain spherical.

2.2. Simulation matrix

In order to establish a matrix of simulation cases, a reasonable range of droplet radii needed to be chosen for a given superficial

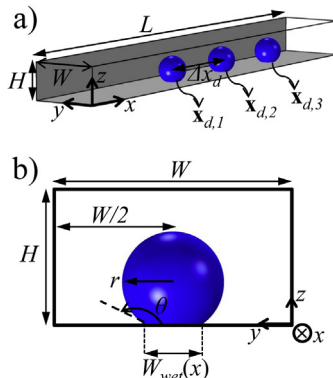


Fig. 1. The representative computational domain (not to scale): a) perspective view, b) yz cross section of the channel at $x_{d,1}$.

Table 1

The fully humidified air properties at 80°C : mass density (ρ) [38], dynamic viscosity (μ) [38], thermal conductivity (k) [38], heat capacity (C_p) [38], and oxygen diffusivity in the air ($D_{O_2-\text{air}}$) [39–41], Prandtl (Pr) and Schmidt (Sc) numbers.

ρ [kg m ⁻³]	μ [μPa s]	$D_{O_2-\text{air}}$ [cm ² s ⁻¹]	k [mW m ⁻¹ °C ⁻¹]	C_p [J kg ⁻¹ °C ⁻¹]	Pr	Sc
0.828	16.253	0.310	26.633	1349.938	0.824	0.633

mean air velocity. The smallest radius for any air velocity is limited by the maximum pore size observed on a GDL surface [11], and this limitation led to 0.10 mm as the minimum radius. As the droplet radius increases for a given air velocity, the droplet shape can deviate from a perfect sphere and droplet adhesion to the GDL–Ch interface can be broken. Both scenarios would void the applicability of the numerical results.

The spherical representation of the droplet can be used when surface tension forces dominate gravitational and inertial forces. The Bond number (Bo) shows the ratio of the gravitational-to-surface-tension forces ($Bo = \rho g r^2 / \sigma$) where g and σ are the gravitational acceleration and air–water surface tension, respectively. For a hydrophobic GDL surface, experiments by Das et al. showed that Bo should be smaller than 0.10 for the gravitational forces to be negligible [34]. The largest Bo, corresponding to $r = 0.20$ mm and $\sigma = 62.6$ mN m^{−1}, was 0.026. Therefore, the droplet shape may be assumed to be independent of the gravitational forces up to $r = 0.20$ mm.

The droplet deformation due to air flow was expressed by Cho et al. as $(r_y - r_x)/r$ where $(r_y - r_x)$ is the mismatch between radii of curvature (r_x and r_y) due to the air drag and r is the original radius in the absence of air flow [27,28]. The ratio of $(r_y - r_x)/r$ as a function of Weber (We) number and channel blockage ratio due to the droplet (ξ) is given by Eq. (1):

$$\frac{r_y - r_x}{r} = \frac{We \xi^2}{4} = \left(\frac{\rho u_m^2 r}{4\sigma} \right) \left(\frac{WH}{WH - r^2(\theta - \cos \theta \sin \theta)} \right)^2 \quad (1)$$

The contact angle (θ) is input to Eq. (1) in radians. The Weber number reflects how dominant the flow inertia is over the droplet-surface-tension forces. The channel blockage ratio accounts for the increasing air velocity due to the limited flow cross section that coincides with the droplet. Table 2 shows the droplet deformation for the entire range of r and u_m . The set of r and u_m parameters that led to a deformation equal to or under 10.5% ($(r_y - r_x)/r \leq 0.105$) was included in the simulation matrix.

The cases that did not lead to a significant droplet deformation were simulated. After conducting single-droplet simulations, numerically calculated drag forces were used to check if the droplets can remain adhered to the GDL–Ch interface. The numerically calculated drag forces were compared against experimentally obtained adhesion forces from the available literature. The droplet-adhesion-force-per-unit-footprint-perimeter was provided by Das et al. for aged SGL 24BA and 24DA GDL samples as 22 and 17 $\mu\text{N mm}^{-1}$, respectively [34]. An average value of 20 $\mu\text{N mm}^{-1}$ was used in the adhesion force calculations. Since the adhesion force is acquired through an experiment with a GDL, the value, and hence the simulation, takes the GDL surface roughness into account. Table 3 shows the numerically calculated drag force (F_x) for each droplet size and superficial mean air velocity. The adhesion forces calculated for the given droplet radius range ($r = 0.10$ – 0.20 mm) are 6.84, 8.21, 10.27, 12.32, and 13.69 μN . The adhesion forces always remained larger than the numerically

Table 2

The droplet deformation $((r_y - r_x)/r)$ as a function of superficial mean air velocity (u_m) and droplet radius (r). The deformations above 0.105 are written with bold text.

r [mm]	u_m [m s ^{−1}]				
	1.59	4.24	7.41	10.59	15.89
0.10	0.001	0.007	0.023	0.047	0.105
0.12	0.001	0.010	0.031	0.063	0.141
0.15	0.002	0.016	0.048	0.097	0.219
0.18	0.004	0.025	0.077	0.158	0.356
0.20	0.005	0.037	0.113	0.230	0.518

Table 3

The numerically obtained air drag on a droplet in the flow direction (F_x [μN]) as a function of superficial mean air velocity (u_m) and droplet radius (r) (The empty boxes indicate the cases that were not simulated due to the deformation in droplet shape.).

r [mm]	u_m [m s ^{−1}]				
	1.59	4.24	7.41	10.59	15.89
0.10	0.21	0.80	1.82	3.16	6.01
0.12	0.34	1.28	2.94	5.11	
0.15	0.66	2.42	5.57	9.69	
0.18	1.32	4.77	10.74		
0.20	2.12	8.20			

obtained drag forces (F_x) in Table 3. Hence, the droplet obstruction method can be used with this simulation matrix.

For the simulations of two droplets, three values of droplet spacing were used, $\Delta x_d = 1.00$, 2.00, and 5.00 mm. The shortest distance between the two droplets was set to be 1.00 mm, which was shown to be possible in the visualization studies of Yang et al. [9] and Zhang et al. [10]. The single-droplet results were analyzed to identify cases that lead to at least a 5% increase in Sh at one of the locations: 1.00, 2.00, and 5.00 mm downstream of the first droplet. Two droplet simulations provided the optimum Δx_d , which would provide the highest Sh downstream of the second droplet. After identifying the optimum Δx_d values for each set of u_m and r , all two droplet cases were simulated again as multiple droplets with the optimum Δx_d . The multiple droplet study provided the maximum Sh to which each case can lead.

2.3. Theoretical foundation for the interfacial transport resistance

In this study, heat (h_T) and mass (h_M) transfer coefficients are together referred to by the variable, ψ . Similarly, thermal conductivity and species diffusivity are referred to by the generic variable, ε . The transport is partially blocked at the GDL–Ch interface by the droplet footprint as previously shown in Fig. 1b. An effective convective transport coefficient (ψ_{eff}) is defined in Eq. (2) to incorporate the values of ψ at dry and droplet-covered GDL–Ch interface in one function.

$$\psi_{\text{eff}}(x, y) = \begin{cases} \text{Dry interface} & \psi \\ \text{Wet interface} & 0 \end{cases} \quad (2)$$

The dry-region-averaged-convective-transport coefficient ($\bar{\psi}(x)$) in Eq. (3) accounts for all ψ_{eff} variations in the y direction by averaging ψ_{eff} over the dry region width ($W - W_{\text{wet}}$):

$$\bar{\psi}(x) = \frac{1}{(W - W_{\text{wet}})} \int_{y=0}^W \psi_{\text{eff}} dy \quad (3)$$

To express $\bar{\psi}$ independent of d_h and ε , the non-dimensional convective transport coefficient ($\Omega(x) = \bar{\psi} d_h / \varepsilon$) is used instead of $\bar{\psi}$. In heat and mass transport applications, Ω represents the Nusselt (Nu) and Sherwood (Sh) numbers, respectively. In the developing flow region and in the flow direction (x), convergence to Ω_{FD} is reached at $1.005\Omega_{\text{FD}}$ value.

3. Numerical approach

In the solution of governing equations, all material properties were assumed to remain constant. Constant air properties allowed the sequential solution of steady-state incompressible Navier–Stokes, conservation of mass, species, and energy equations as provided in Eqs. (4)–(7), respectively.

$$\rho(\mathbf{u} \cdot \nabla) \mathbf{u} = \nabla \cdot \left[-p\mathbf{I} + \mu(\nabla \mathbf{u} + (\nabla \mathbf{u})^T) \right] \quad (4)$$

$$\rho \nabla \cdot \mathbf{u} = 0 \quad (5)$$

$$\nabla \cdot (-D_{O_2\text{-air}} \nabla C + \mathbf{u}C) = 0 \quad (6)$$

$$\rho C_p \mathbf{u} \cdot \nabla T = \nabla \cdot (k \nabla T) \quad (7)$$

Fig. 2 shows a representative reproduction of the mesh for one symmetrical half of the entire geometry. The hollow droplet-shaped obstruction also can be seen. The numerical domain utilized the $y = W/2$ symmetry plane and the droplet obstruction is brought closer to the inlet for better demonstration as shown in Fig. 2. The symmetry plane divides the droplet obstruction in half. The maximum mesh element size (69.1 μm) was obtained after a mesh independency study that will be discussed further in Section 4.1.

For all governing equations, a symmetry boundary condition was imposed at $y = W/2$. Uniform velocity was imposed at the channel inlet ($u = u_m$ at $x = 0$). Zero gauge pressure was imposed as a boundary condition at the outlet ($p = 0$ at $x = 83$ mm). The air flow rates at the inlet and outlet are equal to each other in the simulation since no injection or suction was imposed on the GDL–Ch interface. No-slip boundary condition was imposed on all channel side walls and droplet obstruction surface. The no-slip boundary condition on the droplet surface is representative of the reality based on the experimental velocity measurements within a droplet subjected to air flow in a PEMFC air channel [43]. The liquid water velocity at the droplet–air interface was reported to be at the maximum of 2% of the superficial mean air velocity in the channel [43].

The boundary condition for heat and O_2 transport at the GDL–Ch interface ($z = 0$) was chosen to reflect PEMFC conditions as closely as possible. A spatially varying O_2 flux at the interface can alter the Sherwood number. Although it is known that current density can spatially vary in a PEMFC, it cannot easily be assumed that the O_2 consumption non-uniformity at the reaction sites is translated to the interface since in-plane diffusion in the GDL can lead to a more uniform flux at the interface. The prediction of O_2 flux non-uniformity at the interface deserves a separate in-depth research involving the GDL. Since there is no available Sh data for the condition of a constant O_2 flux at the interface, this numerical study treats the interface with a constant O_2 flux (j) and heat flux (q'').

Heat and O_2 flux values were imposed with large enough values to reduce the calculation errors of the Nusselt and Sherwood numbers, respectively. Theoretically, the Sherwood number is the same for any value of constant O_2 flux at the interface. However, to reduce the numerical errors, O_2 fluxes were imposed proportional with the air velocity. Contrary to variable oxygen flux values, a single heat flux value was imposed, and this choice was entirely based on reducing the maximum error of the Nusselt number that would occur at the highest air velocity. As the air velocity was reduced, the Nusselt number error only became lower. The heat and

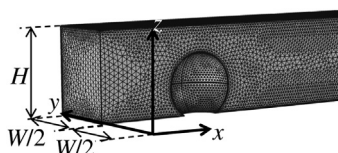


Fig. 2. The meshed domain as a result of mesh independency study (not to scale).

O_2 fluxes were $q'' = 10^3 \text{ W m}^{-2}$ and $j(i) = 0.444 \times 10^{-2}$ to $6.662 \times 10^{-2} \text{ mol m}^{-2} \text{ s}^{-1}$, respectively. The droplet-covered interface did not participate in the heat-mass transfer processes. At a yz cross section with a wet interface, the net energy and oxygen transfer were set to match a fully dry yz cross section by multiplying q'' and j with $(W/(W - W_{\text{wet}}(x)))$. A constant temperature of 80 °C and a constant oxygen concentration of 3.83 mol m^{-3} were imposed at the inlet. Since the resistance to O_2 diffusion through the liquid water droplet dominates the interfacial resistance, O_2 and the equivalent heat transport through the droplet surface was assumed to be zero. Moreover, all side walls of the channel were imposed to have no heat and mass flux.

To comply with the computational limitations, the total length of the simulation domain was divided in the flow direction into three regions of lengths—30 mm, 30 mm, and 23 mm. The velocity, temperature, and concentration profiles at the exit of a region were mapped to the inlet of the successive region. This approach could be applied owing to the absence of backflow where the profile mapping was performed. In the first 60 mm region, the developing flow at channel entrance was simulated and fully developed conditions were achieved. The droplet studies were conducted in the subsequent 23 mm region.

The numerical problem was solved with a commercially available software package, COMSOL Multiphysics® 4.3a. The shape functions for the unknowns \mathbf{u} , C , and T were second order, while the function p was first order. A typical simulation region (three regions form a single case) consists of 1.4M tetrahedral mesh elements and 6.2M degrees of freedom (during the solution of N–S equations). Generalized Minimum Residual Method iterative solver was used along with geometric multigrid scheme. Automatically scaled residuals of unknowns were required to converge to 10^{-6} .

4. Results

In this section, the simulation technique is first validated. Single droplet results show how much Sh can change in the droplet wake. Two droplet results provide information about the effect of spacing on Sh. Multiple droplet results show how Sh progressively changes in the flow direction. All Sh results are accompanied with the ratio of Sh/Nu to show the deviation of heat and mass transfer problems. Since the droplet-affected regions of the channel are the focus of the work, all results are presented by defining 60 mm downstream of the inlet as $x = 0$ mm. Hence, the first droplet position ($x = 63$ mm) is always referred to as $x_{d,1} = 3.00$ mm.

4.1. Mesh independency and model validation

The mesh independency was checked with ten droplets placed in the channel. This scenario was expected to cause a stronger flow disruption compared to a single droplet and thereby be more mesh sensitive. The set of r and u_m leading to the largest droplet-shape deformation, $((r_y - r_x)/r)$, and the smallest possible droplet spacing (Δx_d) was expected to provide the strongest possible flow disruption. Table 2 shows that the largest droplet deformation is led by $r = 0.15$ mm and $u_m = 10.59 \text{ m s}^{-1}$, and, thereby, this set of r and u_m was chosen for the mesh independency check. Moreover, Δx_d was set at 1.00 mm as the shortest droplet spacing. Table 4 presents the mesh cases along with the net drag force on the last droplet in the x direction (F_x). The drag force by Mesh 3 shows mesh independency compared to Mesh 2. In addition to F_x , variations of Sh in the flow direction are analyzed.

Fig. 3a shows the overall trends of Sh due to ten droplets in a row. Multiple flow disruptions by the droplets cause a gradual increase in Sh, and it reaches an asymptotic value after the seventh droplet. Fig. 3b shows Sh in the vicinity of the tenth droplet

Table 4

The mesh cases used in the mesh independency study and the drag forces on the last droplet in the flow direction.

Mesh case	Number of elements	Max. element size [μm]	Drag on the droplet, F_x [μN]
1	317,045	121.5	8.84
2	569,814	98.7	9.23
3	1,389,663	69.1	9.28

($x_{d,10} = 12.00$ mm). Meshes 2 and 3 show almost no difference in the results. Since computational resources were available for Mesh 3, a conservative approach was taken and Mesh 3 was chosen in all simulations.

Mesh 3 was validated with the use of Nu and Poiseuille number (Po) in the fully developed region. Upstream of the first droplet, Sh_{FD} and Nu_{FD} were obtained to be 3.349, which matches with $Nu_{FD} = 3.584$ from the numerical study of Dharaiya and Kandlikar with 6.6% error [44]. Moreover, Po_{FD} was reported by Shah and

Sekulic [45] to be 15.127 for the simulated channel cross section. This value agrees very well with the simulated value of 15.155 with a difference of only 0.2%.

4.2. Single droplet results

Fig. 4a shows variations of Sh in the flow direction as a function of u_m at $r = 0.15$ mm. The Sherwood number goes through a maximum, then a minimum, followed by another maximum. The maximum Sh downstream of the droplet is referred to as $Sh_{1,max}$ and is significant as it indicates how far downstream the droplet effect persists. At the lowest u_m , there is no detectable overshoot of Sh downstream of the droplet. It can be inferred that there is a need for a minimum u_m to achieve an overshoot of Sh.

Fig. 4b demonstrates how much the equivalent heat and mass transfer results deviate by using the ratio of the Sherwood to Nusselt number (Sh/Nu). Upstream of the droplet Sh/Nu is equal to unity since the flow is in the fully developed condition. At the droplet position ($x_{d,1} = 3$ mm), Sh/Nu becomes smaller than unity with a dramatic change of which intensity is proportional with the air velocity (u_m). The case $u_m = 4.24$ m s⁻¹ shows a steady recovery of Sh/Nu to unity downstream of the droplet. However, the cases $u_m \geq 7.49$ m s⁻¹ do not show a steady recovery in the immediate

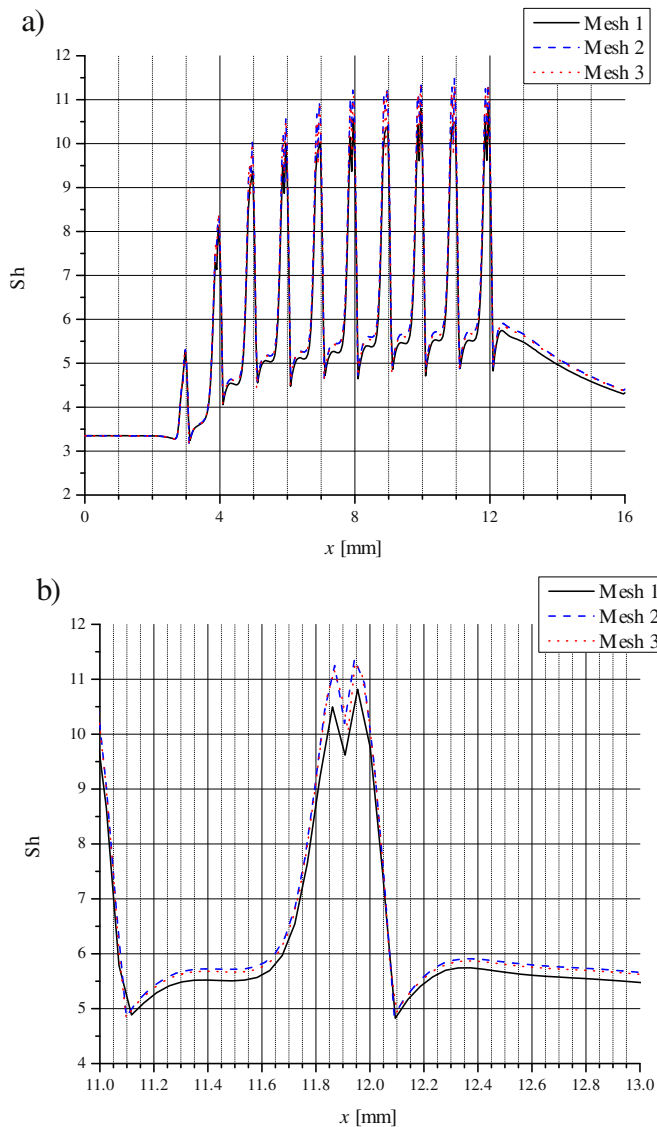


Fig. 3. The mesh independency study with ten droplets in a row (first droplet position, $x_{d,1} = 3.00$ mm, and droplet spacing, $\Delta x_d = 1.00$ mm): a) overview of the Sherwood number (Sh), b) close-up view to Sh in the vicinity of the tenth droplet ($x = 12.00$ mm).

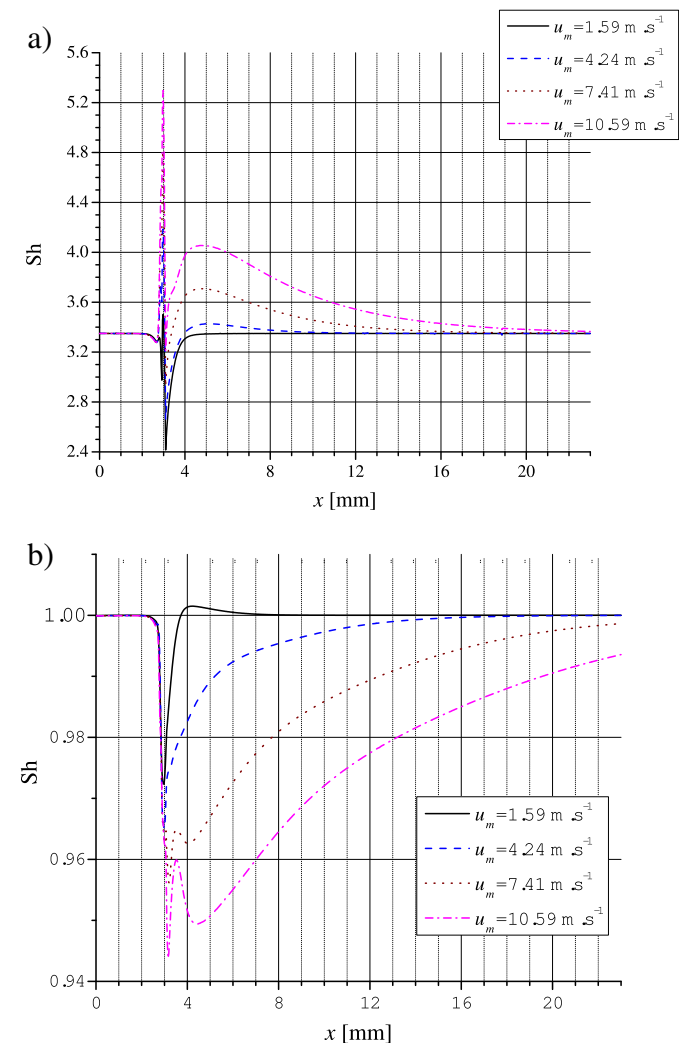


Fig. 4. The effect of superficial mean air velocity (u_m) on the a) Sherwood number (Sh), and b) Sherwood/Nusselt number ratio (Sh/Nu) for the droplet radius, $r = 0.15$ mm (the droplet position, $x_{d,1} = 3.00$ mm).

droplet wake. Moreover, the case $u_m = 1.59 \text{ m s}^{-1}$ leads to Sh/Nu values larger than unity. These trends will be further discussed in Section 5.

Table 5 shows the values of $Sh_{1,max}$ and the shaded boxes indicate the cases not leading to any overshoot of Sh downstream of a droplet. The case $u_m = 10.59 \text{ m s}^{-1}$ and $r = 0.15 \text{ mm}$ leads to the highest $Sh_{1,max}$ along with the lowest Sh/Nu . All tabulated values of $Sh_{1,max}$ increase with r and u_m except in one case ($u_m = 4.24 \text{ m s}^{-1}$ and $r = 0.18 \text{ mm}$). This irregularity will be discussed in Section 5.

The data in Table 5, with the exception of values for $r = 0.20 \text{ mm}$, is correlated by the following equations with a maximum deviation of 0.657%:

$$Sh_{1,max}(u_m, r) = f(r) + g(r)u_m \quad (8)$$

$$f(r) = -113.67r^2 + 21.968r + 2.2657 \quad (9)$$

$$g(r) = -219.03r^3 + 113.67r^2 - 16.211r + 0.7119 \quad (10)$$

The units of u_m and r are m s^{-1} and mm respectively.

4.3. Two-droplet results

Two droplet studies were conducted to show the effect of droplet spacing on Sh . The goal was to present relatively large increases in Sh values in the wake of both droplets to easily highlight how much Sh can differ in PEMFC air flow channels. Hence, the cases to be simulated in this section were chosen according to the Sh values downstream of the single-droplet cases. Locations of 1.00, 2.00, and 5.00 mm downstream of the droplet were checked for at least 5% of Sh increase. The cases satisfying this condition at one of the checked locations were $u_m = 7.41 \text{ m s}^{-1}$ for $r = 0.15$ and 0.18 mm , and $u_m = 10.59 \text{ m s}^{-1}$ for $r = 0.12$ and 0.15 mm .

Fig. 5 demonstrates the effect of droplet spacing on Sh and Sh/Nu for the case $u_m = 10.59 \text{ m s}^{-1}$ and $r = 0.15 \text{ mm}$. Fig. 5a shows the overshoot of Sh at the wake of the second droplet ($Sh_{2,max}$) and $Sh_{2,max}$ is used to compare the effect of spacing in different cases. The effect of droplet spacing on Sh was consistent among all sets of u_m and r . The droplet spacing $\Delta x_d = 2.00 \text{ mm}$ leads to the highest $Sh_{2,max}$, followed by the spacing values of $\Delta x_d = 5.00 \text{ mm}$ and 1.00 mm .

Fig. 5b presents the corresponding Sh/Nu results. In single-droplet results, Sh and Sh/Nu were inversely related. However, the trends downstream of the second droplet do not show a parallelism with the previously reported results. The droplet spacing of $\Delta x_d = 2.00 \text{ mm}$ and 5.00 mm lead to smaller Sh/Nu values compared to $\Delta x_d = 1.00 \text{ mm}$. This observation is in agreement with the previously reported inverse proportionality between Sh and Sh/Nu . However, the Sh/Nu values at $\Delta x_d = 2.00 \text{ mm}$ and 5.00 mm are almost the same despite Sh being clearly higher at

Table 5

The maximum Sh downstream of a droplet ($Sh_{1,max}$) as a function of superficial mean air velocity (u_m) and droplet radius (r) (The shaded boxes indicate the cases with no overshoot of Sh in the droplet wake. The grey boxes indicate the cases that were not simulated due to droplet deformation.)

		$u_m [\text{m.s}^{-1}]$				
		1.59	4.24	7.41	10.59	15.89
$r [\text{mm}]$	0.10		3.362	3.385	3.412	3.461
	0.12		3.379	3.449	3.538	
	0.15		3.428	3.710	4.055	
	0.18		3.391	4.001		
	0.20	3.353	3.465			

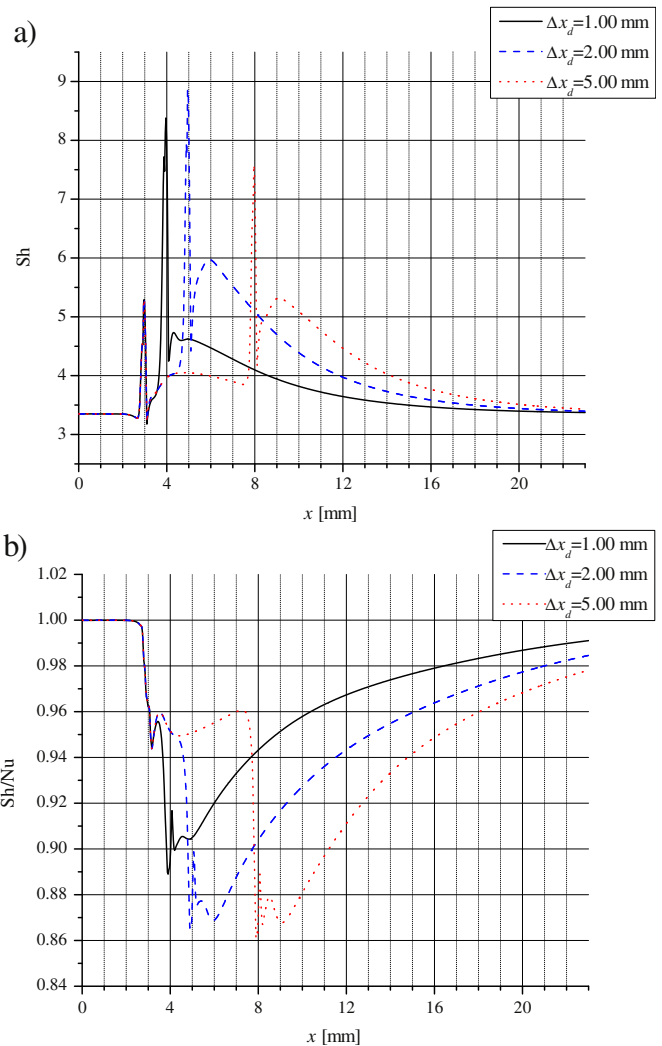


Fig. 5. The effect of droplet spacing (Δx_d) on the a) Sherwood number (Sh) and b) Sherwood/Nusselt number ratio (Sh/Nu) for two consecutive droplets at the superficial mean air velocity, $u_m = 10.59 \text{ m s}^{-1}$ and the droplet radius, $r = 0.15 \text{ mm}$ (the first and the second droplet positions: $x_{d,1} = 3 \text{ mm}$ and $x_{d,2} = x_{d,1} + \Delta x_d$, respectively).

$\Delta x_d = 2.00 \text{ mm}$ than $\Delta x_d = 5.00 \text{ mm}$. The reason behind this trend will be explained in Section 5.

To characterize the effect of droplet spacing, overshoot values of Sh in the two droplet wakes ($Sh_{N,max}$) were compared against each other by defining a Sh enhancement factor ($Sh_{2,max}/Sh_{1,max}$). Table 6 shows this enhancement factor of Sh by the second droplet. The highest enhancement factor among all was achieved by the case $u_m = 10.59 \text{ m s}^{-1}$, $r = 0.15 \text{ mm}$, and $\Delta x_d = 2.00 \text{ mm}$. For each condition of u_m and r , the highest respective enhancement factor was achieved when $\Delta x_d = 2.00 \text{ mm}$. The second highest enhancement factor for a particular u_m and r condition was not consistently achieved by $\Delta x_d = 1.00 \text{ mm}$ or 5.00 mm . Only the condition of $u_m = 7.41 \text{ m s}^{-1}$ and $r = 0.18 \text{ mm}$, $\Delta x_d = 1.00 \text{ mm}$ led to the second highest enhancement factor.

4.4. Multiple-droplet results

Multiple-droplet studies show the progressive change of Sh in the flow direction due to eleven droplets. All sets of u_m and r from the two-droplet simulations were transferred to multiple-droplet investigations with the optimum droplet spacing for Sh enhancement ($\Delta x_d = 2.00 \text{ mm}$). Fig. 6 illustrates the sequential impact of

Table 6

The enhancement factor of Sh by the second droplet ($Sh_{2,max}/Sh_{1,max}$) as a function of droplet spacing (Δx_d) and given for different superficial mean air velocity (u_m) and droplet radius (r) cases.

	Δx_d [mm]		
	1.00	2.00	5.00
$u_m = 7.41 \text{ m s}^{-1}$ and $r = 0.15 \text{ mm}$	1.081	1.194	1.093
$u_m = 7.41 \text{ m s}^{-1}$ and $r = 0.18 \text{ mm}$	1.140	1.249	1.113
$u_m = 10.59 \text{ m s}^{-1}$ and $r = 0.12 \text{ mm}$	1.052	1.133	1.088
$u_m = 10.59 \text{ m s}^{-1}$ and $r = 0.15 \text{ mm}$	1.141	1.473	1.311

each droplet on Sh and Sh/Nu. Towards the end of the channel, the values in between two consecutive droplets start showing a pattern. Values in between the tenth and the eleventh droplets ($21 \text{ mm} \leq x \leq 23 \text{ mm}$) were averaged in the flow direction into Sh_{av} and $(Sh/Nu)_{av}$ from Fig. 6a and b, respectively.

Fig. 6a shows the evolution of Sh in the flow direction, and this evolution is almost complete by the sixth droplet. Table 7 shows the values of Sh_{av} , and this data is further analyzed to find a parallelism

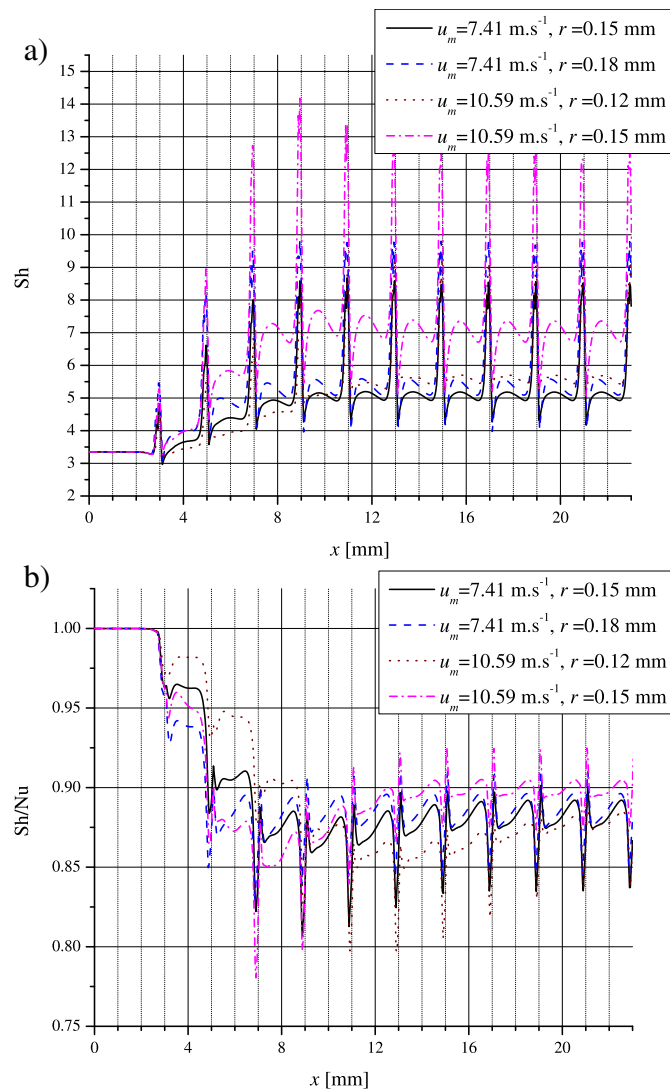


Fig. 6. a) The effect of superficial mean air velocity (u_m) and droplet radius (r) on the a) Sherwood number (Sh) and b) Sherwood/Nusselt number ratio (Sh/Nu) for eleven droplets in a row (positions for the first and Nth droplet ($N > 1$): $x_{d1} = 3.00 \text{ mm}$ and $x_{dN} = x_{d,N-1} + 2.00 \text{ mm}$, respectively).

between the Sh enhancement factor by the second droplet with $\Delta x_d = 2.00 \text{ mm}$ (from Table 6) and Sh_{av} . Except for the case of $u_m = 10.59 \text{ m s}^{-1}$ and $r = 0.12 \text{ mm}$, there is a parallelism between the enhancement factor and Sh_{av} . Although the case $u_m = 10.59 \text{ m s}^{-1}$ and $r = 0.12 \text{ mm}$ has the lowest enhancement factor, the corresponding Sh_{av} leads the second highest value. In summary, enhancement factors from two-droplet studies cannot be used as a predictive tool for the average Sh far downstream of multiple droplets.

Fig. 6b shows the Sh/Nu ratio corresponding to the values in Fig. 6a. Fig. 6b is analyzed to find parallelisms between Sh and Sh/Nu. The gradual decrease of Sh/Nu reaches a plateau by the ninth droplet. Although this trend resembles the plateau of Sh in Fig. 6a, there is a major difference between Fig. 6a and b: none of the family of plots in Fig. 6a, except $u_m = 10.59 \text{ m s}^{-1}$ and $r = 0.12 \text{ mm}$, crosses each other. However, the family of plots in Fig. 6b crosses each other as they evolve in the flow direction. The minimum $(Sh/Nu)_{av}$ is a result of the case $u_m = 10.59 \text{ m s}^{-1}$ and $r = 0.12 \text{ mm}$ and was calculated to be 0.876. Since this case does not lead to the highest Sh_{av} , it can be inferred that there is no clear correlation between Sh and Sh/Nu.

5. Discussion

5.1. The effect of a droplet on the velocity and O_2 concentration profiles

To understand the reported results in Sections 4.2 and 4.3, the following additional background provides useful insight. In this numerical study, the enforced constant flux boundary condition ensures a set O_2 concentration and temperature gradient at the GDL–Ch interface. The mean O_2 concentration and temperature of the flow are independent of flow conditions and will change linearly in the flow direction. The only unknowns required to calculate Sh and Nu are the concentration and temperature values at the interface, respectively. These values are dependent on the local flow conditions and calculated numerically. The Sherwood number is calculated to be higher with the increasing interfacial concentration. Since the transport of concentration and temperature are analogous, only velocity and concentration fields will be analyzed. Fig. 7 shows how a droplet affects the air flow in the case $u_m = 10.59 \text{ m s}^{-1}$ and $r = 0.15 \text{ mm}$. While Fig. 7a focuses on the velocity field, Fig. 7b complements the understanding of Fig. 7a with the concentration field.

Fig. 7a shows a map of the velocity magnitude in the $+x$ direction at given slices that are separated from each other by 0.20 mm . The regions in slices with an incomplete filling correspond to a flow in the $-x$ direction (flow reversal). The flow reversal can be seen at slices $x = 2.80, 3.20$ and 3.40 mm . The arrows on the slices show the direction of the flow in the yz plane. The lengths of the arrows are logarithmically proportional to the velocity magnitude in a yz cross section. The air closer to the symmetry line on the interface ($y = W/2$ and $z = 0$) is brought back from $x = 3.40 \text{ mm}$ towards the droplet and recirculated back to the high velocity region at $x = 3.20 \text{ mm}$. The high velocity region is directed towards the symmetry line on the interface ($-z$ direction). Moreover, downstream of $x = 3.40 \text{ mm}$,

Table 7

The effect of superficial mean air velocity (u_m) and droplet radius (r) on the flow direction averaged Sh (Sh_{av}).

$u_m = 7.41 \text{ m s}^{-1}$, $r = 0.15 \text{ mm}$	$u_m = 7.41 \text{ m s}^{-1}$, $r = 0.18 \text{ mm}$	$u_m = 10.59 \text{ m s}^{-1}$, $r = 0.12 \text{ mm}$	$u_m = 10.59 \text{ m s}^{-1}$, $r = 0.15 \text{ mm}$
5.383	5.789	5.891	7.466

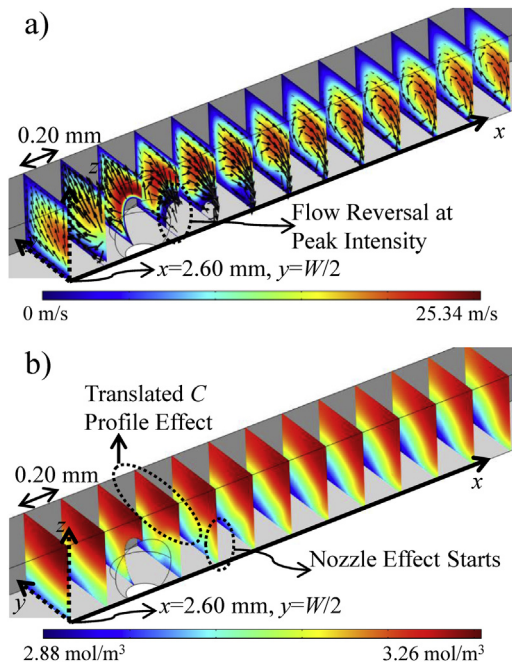


Fig. 7. The flow conditions for the superficial mean air velocity $u_m = 10.59 \text{ m s}^{-1}$, and the droplet radius, $r = 0.15 \text{ mm}$ yz direction of the velocity is shown by arrows of which lengths are logarithmically proportional with the velocity magnitude in the yz cross section. Each slice is separated for 0.20 mm , and the colour map corresponds to a) $+x$ velocity magnitude ($-x$ velocity areas are left blank on the slices), and b) O_2 concentration (C). (For interpretation of the references to colour in this figure legend, the reader is referred to the web version of this article.)

the air starts to recirculate around the $+x$ axis close to the symmetry line on the interface.

Fig. 7b shows the impact of the velocity field on the concentration profile. Upstream of the droplet, the concentration does not show a significant variation along the channel width (the y direction). However, in the immediate droplet wake ($x = 3.20 \text{ mm}$), the symmetry line and channel corner on the interface ($y = W$ and $z = 0$) show a lower concentration of O_2 . The low concentration leads to a reduction in Sh . The shifting of the high concentration region away from the interface is referred to here as the translated concentration profile effect. The O_2 rich air closer to the top channel wall ($z = H$) is directed to the symmetry line on the interface by a strong convection at $x \geq 3.40 \text{ mm}$. The strong convection that brings O_2 -rich air towards the interface is referred to here as the nozzle effect. In the flow direction, the nozzle effect transforms into a recirculation around $+x$ axis. The recirculation distributes O_2 towards the channel bottom corner. The Sherwood number increases as a result of the aforementioned convective effects. The recirculation does not affect the channel corners strongly. Hence, the recovery of the O_2 profile at the bottom channel corner depends on the diffusion more than at the symmetry line.

5.2. Comparison of heat and mass transfer results

In Sections 4.2–4.4, it has been shown that the equivalent heat and mass transfer problems led to the same interfacial resistance in a fully developed flow region. However, the flow disruption by the droplets caused a deviation in the interfacial resistances of heat and mass transfer problems. The deviations between the results of heat and mass transfer problems can be explained with the effect of a droplet on the velocity and O_2 concentration profiles. The deviation in the results of these two equivalent problems can be seen in

regions of developing flow, and the magnitude of the deviation is proportional with the mismatch between the Schmidt and Prandtl numbers. Since in this problem the Schmidt number is smaller than the Prandtl number, a higher O_2 diffusivity is available compared to the equivalent thermal diffusivity. Considering this Schmidt and Prandtl mismatch, the effect of the observed velocity field on the Sh – Nu deviation will be discussed.

Under the given constant O_2 flux boundary condition, a high Sh is equivalent to a small difference of O_2 concentration calculated in between the GDL–Ch interface and the mean flow. A higher concentration in the vicinity of the interface corresponds to a smaller concentration difference. The translated concentration profile effect increases the concentration difference since the O_2 concentration is reduced in the vicinity of the interface. Contrarily, the nozzle effect brings the high O_2 concentration back to the interface and decreases the concentration difference.

The impact of the translated concentration/temperature profile and the nozzle effect on the Sherwood/Nusselt number vary with different diffusivities of O_2 /heat. The translated concentration profile effect is recovered by diffusion or convection along the channel height (z direction) depending on the position in the channel. Until the translated concentration effect is fully recovered, both transport mechanisms will contribute to the increase in the concentration near the interface. When the convective effects are weak, the diffusion is more responsible for the recovery of the translated concentration profile effect. From the droplet up to where the nozzle effect starts, the flow reversal is strong and the convective effects in the $-z$ direction are weak in the vicinity of the interface. The higher O_2 diffusivity compared to the thermal diffusion will allow Sh to increase faster than Nu in regions where the translated concentration profile is being yet recovered. Therefore, Sh can remain higher than Nu in the regions where the concentration profile still requires adjustment with the aid of diffusion to provide higher O_2 to the interface.

In the regions where the translated concentration profile effect is recovered, convection can bring O_2 rich air to the GDL–Ch interface, and this increases Sh above the fully developed value. The O_2 consumption and the consequent diffusion at the interface counteracts this convection dominated concentration profile. As the convection weakens in the flow direction, the higher diffusivity leads to a faster recovery of the concentration profile back to the fully developed one. Since the O_2 diffusivity is higher than the thermal diffusivity, Sh is expected to recover to the fully developed value faster than Nu . Therefore, Nu can remain higher than Sh in the regions where the convective effects (such as the nozzle effect) are strong.

5.3. The interpretation of the results with the heat/mass transfer analogy

After mapping the velocity profile changes into deviations of heat/mass transfer results, some example cases are analyzed to check how well the mapping works. Fig. 8 depicts Sh for the superficial mean air velocity 4.24 m s^{-1} with a variable droplet size. In this case, the maximum Sherwood number in the droplet wake ($Sh_{1,\max}$) does not consistently increase with r as seen in other cases. Fig. 8a shows that $Sh_{1,\max}$ decreases from $r = 0.15 \text{ mm}$ to 0.18 mm and reaches to the maximum at $r = 0.20 \text{ mm}$. Fig. 8b shows Sh/Nu with a faster rate of increase at the immediate droplet wake as the droplet size increases. This is correlated with an intensified translated concentrated profile effect due to the increased droplet size and weakened convective effects in the $-z$ direction.

The nozzle effect is expected to be weaker at $r = 0.18 \text{ mm}$ since $Sh_{1,\max}$ is smaller at $r = 0.18 \text{ mm}$ compared to $r = 0.15 \text{ mm}$. The velocity field analysis of the $r = 0.18 \text{ mm}$ case showed two

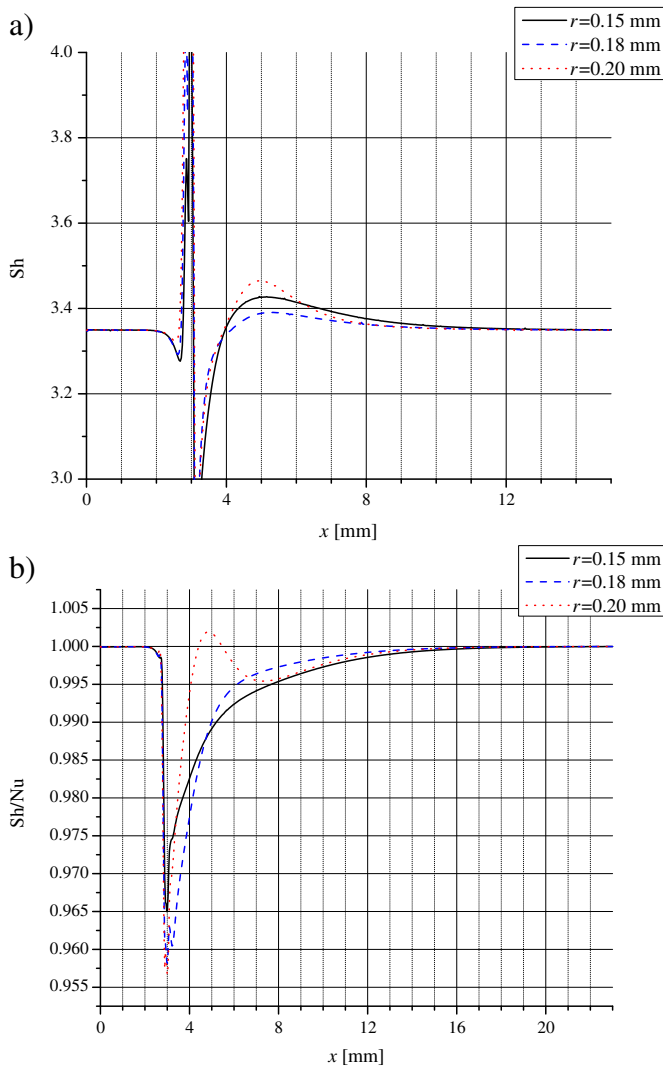


Fig. 8. The effect of droplet size (r) on the a) Sherwood number (Sh), b) Sherwood/Nusselt number ratio (Sh/Nu) at superficial mean air velocity $u_m = 4.24 \text{ m s}^{-1}$ (droplet position, $x_{d,1} = 3.00 \text{ mm}$). In panel a full extent of values were cropped to focus to $x = 5.00 \text{ mm}$).

recirculations at the same yz cross sections in the droplet wake. While the recirculation closer to the interface was around the $+x$ axis, the other one was closer to the top channel wall and around the $-x$ axis. Two recirculations cannot bring the O_2 -rich air from the vicinity of the top channel wall to the interface. Hence, this case led to the smallest $Sh_{1,max}$. The case with the largest droplet size, $r = 0.20 \text{ mm}$, led to a single recirculation around the $-x$ axis, which is the opposite direction of the one in the case $r = 0.15 \text{ mm}$. The recirculation at $r = 0.20$ created a strong nozzle effect and, hence, led to the highest $Sh_{1,max}$. The strong nozzle effect can also be seen in Fig. 8b for $r = 0.20 \text{ mm}$ at $x > 5.00 \text{ mm}$, which indicates the change of Sh/Nu towards a value smaller than unity. It can be concluded that the recirculation downstream of the droplet changes direction at $r = 0.18 \text{ mm}$. The change of recirculation direction weakens the convective effects and decreases $Sh_{1,max}$ at a critical droplet size.

The impact of flow reversal on Sh/Nu ratio can also be observed in Fig. 4b. Plots for superficial air velocities, 7.41 m s^{-1} , and 10.59 m s^{-1} depict a local maximum at $x \approx 3.50 \text{ mm}$. In the immediate vicinity of the droplet, the flow reversal becomes stronger

with the air velocity, and this leads to a larger local maximum of Sh/Nu . In the case $u_m = 1.59 \text{ m s}^{-1}$, Sh/Nu overshoots to a value larger than unity and then recovers to unity in the flow direction. The boundary layer separation in the droplet wake is insignificant and the nozzle effect is negligible. Thereby, the translated concentration profile is recovered by the diffusion only. Hence, Sh approaches the fully developed value faster than Nu owing to the higher mass diffusion than thermal diffusion.

The analysis of the single-droplet case can be used towards the results of two consecutive droplets. It was shown that the translated concentration profile effect can be recovered by the nozzle effect after a certain distance downstream of the droplet. If the spacing of the droplets is kept under the optimum value (2.00 mm), the concentration profile is translated by the second droplet for the second time before the O_2 -rich air reaches from the top channel wall to the GDL–Ch interface. In this case, the interface cannot fully utilize the O_2 -rich air flow. The recirculation around the $+x$ axis downstream of the second droplet also was compared for $\Delta x_d = 1.00$ and 2.00 mm . The axis of recirculation for $\Delta x_d = 2.00 \text{ mm}$ is much closer to the interface. Hence, it can increase Sh to higher values.

For the spacing values of $\Delta x_d = 2.00$ and 5.00 mm , the maximum Sh in the second droplet wake was higher at $\Delta x_d = 2.00 \text{ mm}$. However, the corresponding Sh/Nu values were found to be almost the same. The spacing of 2.00 mm results in a higher Sh at every point along the channel width than the spacing 5.00 mm . This means that every point along the channel width has a smaller concentration drop when the spacing is 2.00 mm compared to 5.00 mm . The spacing 5.00 mm shows a smaller Sh/Nu in the vicinity of the symmetry line than the spacing 2.00 mm . This is correlated with the fact that the recirculation in spacing 5 mm imposes a concentration gradient in the z direction initially increasing towards the top channel wall compared to a steady decrease in the gradient in the spacing 2.00 mm . Retaining this increasing gradient is possible by a low diffusivity which is provided in the heat transfer case. Hence, Sh/Nu is lower in the aforementioned region.

Towards the channel corner at the interface, the spacing 5.00 mm shows a larger Sh/Nu than the spacing 2.00 mm . Both spacing values have a steady decrease in the concentration gradient in the z direction. However, in the spacing 2.00 mm , the decrease in concentration gradient transforms into a sharp increase towards the top wall of the channel. This increase in the gradient can bring more O_2 towards the interface as the convective effects weaken. Hence, the mass transfer case with more diffusivity leads to an Sh/Nu ratio larger in 5 mm than 2 mm in the aforementioned region.

Under the light of analyzing Sh/Nu in the second droplet wake for spacing values of 2.00 mm and 5.00 mm , it can be concluded that in both cases, the Sh/Nu ratio has the same average value along the channel width. However, because of the change in local flow conditions, the variations of Sh/Nu values along the channel width are different.

5.4. Applicability of results at different PEMFC operating conditions

PEMFCs can operate at a wide range of temperatures and relative humidity values. These two conditions can change even within the same channel in the flow direction. Therefore, it is important to know the extent of applicability for the Sh results presented in this article. The applicability of Sh is directly dependent on the Schmidt number. As the difference between the Schmidt number in this work and the target application grows, the Sherwood number results become less applicable. As a reference, PEMFCs operating with fully humidified air can have a range of Schmidt number 0.752 – 0.633 for the temperature range 20 – 80°C .

The heat transfer results for the Prandtl number ($Pr = 0.824$) can be interpreted as a PEMFC operating at $Sc = 0.824$. Therefore, the reported deviations of Sh and Nu can be used as a benchmark for the applicability of the Sh results. For instance, a PEMFC operating at $20\text{ }^{\circ}\text{C}$ and with fully humidified air can use the Sh results in this paper with a smaller error than the presented maximum Sh/Nu ratio.

5.5. Estimation of the effect of the Sherwood number variations on cell performance

In order to discuss the impact of droplet presence in the air channel on cell performance, it can be useful to initially present the effect of interfacial O_2 transport resistance on the performance. Since the cell performance is partially dependent on O_2 concentration at the catalyst layer (CL), two comparative cases will be presented to show how interfacial O_2 transport resistance will lower the cell voltage at a given current density by decreasing the O_2 concentration at CL.

The concentration drop from the air channel to CL will be calculated through the sum of two components: 1) concentration drop in the GDL (ΔC_{GDL}), and 2) concentration drop at the GDL–Ch interface (ΔC_{GDL-Ch}). The GDL is assumed to be $200\text{ }\mu\text{m}$ thick (t) and subjected to Fick's diffusion. Under these conditions, concentration drop in the GDL can be calculated through $\Delta C_{GDL} = j/(D_{O_2-GDL} \times t)$ along with the estimated O_2 diffusivity in the GDL (D_{O_2-GDL}) $D_{O_2-GDL} = D_{O_2-air}/1.5$ [40]. The concentration drop at the interface can be calculated through $\Delta C_{GDL-Ch} = j/h_M$ where the mass transfer coefficient was previously defined as $h_M = Sh \times D_{O_2-air}/d_h$.

The largest variations in Sh were seen at the superficial mean velocity 10.59 m s^{-1} , which is equivalent to 1.0 A cm^{-2} . At this current density, the variation of voltage due to a change in O_2 concentration from state 1 to state 2 can be calculated through Eq. (11) [40] where R_u and F_c are universal gas constant and Faraday's constant.

$$\Delta V_{1-2} = \frac{R_u T}{F_c} \ln \left[\frac{C_2}{C_1} \right] \quad (11)$$

The O_2 concentration at the inlet 3.83 mol m^{-3} leads to 1.92 mol m^{-3} in the vicinity of channel exit since the stoichiometry is 2. If only the O_2 concentration drop in the GDL is accounted for, and the interfacial drop is neglected, concentration at the CL becomes $C_{CL} = 1.49\text{ mol m}^{-3}$. By using the fully developed Sh and the largest Sh values from single, two and multiple droplet results, the concentration drop at the interface can be respectively calculated as $\Delta C_{GDL-Ch} = 0.22, 0.18, 0.12$ and 0.10 mol m^{-3} .

By using the calculated values above and Eq. (11), the voltage drop due to the inclusion of fully developed interfacial oxygen transport resistance to GDL resistance is 4.8 mV . The maximum Sh obtained by a single, two and multiple droplets can reduce this voltage loss with the respective values: $0.9, 2.2$, and 2.8 mV . Hence, the voltage drop due to the fully developed interfacial oxygen transport resistance can be recovered up to 58% by the presence of multiple droplets in the channel.

6. Conclusions

The interfacial O_2 transport resistance in PEMFC air flow channels was investigated through a numerical approach. The results were reported in terms of the non-dimensional Sherwood number (Sh). It was postulated that the presence of droplets in a channel would affect Sh significantly. This effect was investigated by mimicking the flow by the use of droplet-shape obstructions in the channel. Sets of superficial mean air velocity (u_m) and droplet

radius (r) were simulated in such a way that adhesion and spherical shape of droplets would not be violated. Moreover, fully humidified and $80\text{ }^{\circ}\text{C}$ air properties were used. Under these conditions, the droplets were shown to increase Sh compared to the fully developed value (Sh_{FD}).

- Sh starts showing an increase in the droplet wake when air velocity reaches the minimum value for a given droplet radius. The increase in Sh is intensified with air velocity, droplet radius, and the number of droplets in a row.
- A correlation was provided to predict the maximum possible Sh downstream of a single droplet. The maximum possible increase of Sh was reported to be 21% .
- A sequence of two droplets was investigated to understand the effect of droplet spacing on Sh . Among the investigated spacing values of $1.00, 2.00$ and 5.00 mm , 2.00 mm spacing was found to lead to the highest Sh increase in the second droplet wake. This highest increase corresponds to 78% .
- The effect of multiple droplets in a row was investigated with eleven droplets that were spaced with the optimum spacing (2 mm) found in the study. It was shown that after the sixth droplet, the Sh profile in between two consecutive droplets did not present a change at the next set of two droplets. The Sherwood number was averaged in between the last two droplets in the flow direction. The highest average Sh corresponded to an increase of 122% .
- The heat and mass transfer analogy was analyzed by simulating the equivalent heat transfer problem in the same channel geometry. The Sherwood and Nusselt (Nu) numbers match under fully developed flow conditions. When the flow is disrupted by droplets, Sh and Nu start diverging proportional to the difference between the Schmidt and Prandtl numbers and the intensity of flow disruption.
- The average deviation of Sh and Nu between two consecutive droplets remains constant after the ninth droplet in multiple-droplet studies. The maximum average $Sh-Nu$ deviation was reported to be $Sh/Nu = 0.876$ for the air velocity 10.59 m s^{-1} and a droplet size of 0.12 mm .
- The applicability of the Sh results from this study to an application is dependent on the difference between the Schmidt number (Sc) used here and the Sc in the application. The results of Sh were obtained with $Sc = 0.633$. As the Sc in the desired application deviates from 0.633 , the results from this study are less applicable. The results of the Nusselt number with the Prandtl number 0.824 can be interpreted as Sh at $Sc = 0.824$. Therefore, the deviations of Sh and Nu in this work can be utilized as a benchmark for the Sh applicability at different Sc values.

Acknowledgements

This work was conducted in the Thermal Analysis, Microfluidics, and Fuel Cell Laboratory in the Mechanical Engineering Department at Rochester Institute of Technology. Support for this project was provided by the U.S. Department of Energy under award number: DE-EE0000470. Discussions with Wenbin Gu and Jeffrey Gagliardo from General Motors Electrochemical Laboratory at Honeoye Falls, NY are gratefully acknowledged.

References

- [1] W. Gu, D.R. Baker, Y. Liu, H.A. Gasteiger, in: W. Vielstich, H. Yokokawa, H.A. Gasteiger (Eds.), *Handbook of Fuel Cells – Fundamentals, Technology and Applications*, vol. 6, John Wiley & Sons, England, 2009, pp. 631–657.
- [2] K. Tüber, D. Póca, C. Hebling, J. Power Sources 124 (2003) 403–414.
- [3] U. Pasaogullari, C.Y. Wang, J. Electrochem. Soc. 151 (3) (2004) A399–A406.

- [4] U. Pasaogullari, C.-Y. Wang, K.S. Chen, J. Electrochem. Soc. 152 (8) (2005) A1574–A1582.
- [5] Z.H. Wang, C.Y. Wang, K.S. Chen, J. Power Sources 94 (2001) 40–50.
- [6] K.-T. Jeng, C.-Y. Wen, L.D. Anh, J. Mech. 23 (4) (2007) 275–284.
- [7] H. Hassanzadeh, X. Li, J.J. Baschuk, S.H. Mansouri, Int. J. Energy Res. 35 (2011) 670–689.
- [8] M.I. Rosli, D.J. Borman, D.B. Ingham, M.S. Ismail, L. Ma, M. Pourkashanian, J. Fuel Cell Sci. Technol. 7 (2010) 061015-1–061015-7.
- [9] X.G. Yang, F.Y. Zhang, A.L. Lubawy, C.Y. Wang, ECS Solid State Lett. 7 (11) (2004) A408–A411.
- [10] F.Y. Zhang, X.G. Yang, C.Y. Wang, J. Electrochem. Soc. 153 (2) (2006) A225–A232.
- [11] A. Theodorakakos, T. Ous, M. Gavaises, J.M. Nouri, N. Nikolopoulos, H. Yanagihara, J. Colloid Interface Sci. 300 (2006) 673–687.
- [12] D. Spornjak, A.K. Prasad, S.G. Advani, J. Power Sources 170 (2007) 334–344.
- [13] E. Kimball, T. Whitaker, I.G. Kevrekidis, J.B. Benziger, ECS Trans. 11 (1) (2007) 725–736.
- [14] I.S. Hussaini, C.-Y. Wang, J. Power Sources 187 (2009) 444–451.
- [15] J.M. Sergi, S.G. Kandlikar, Int. J. Hydrogen Energy 36 (2011) 12381–12392.
- [16] K. Takada, Y. Ishigami, J. Inukai, Y. Nagumo, H. Takano, H. Nishide, M. Watanabe, J. Power Sources 196 (2011) 2635–2639.
- [17] D. Lee, J. Bae, Int. J. Hydrogen Energy 37 (2012) 422–435.
- [18] K. Nishida, S. Tanaka, S. Tsushima, S. Hirai, ECS Trans. 41 (1) (2011) 419–428.
- [19] K.S. Chen, M.A. Hickner, D.R. Noble, Int. J. Energy Res. 29 (2005) 1113–1132.
- [20] L. Hao, P. Cheng, Int. J. Heat Mass Transfer 53 (2010) 1243–1246.
- [21] A.D. Le, B. Zhou, H.-R. Shiu, C.-I. Lee, W.-C. Chang, J. Power Sources 195 (2010) 7302–7315.
- [22] X. Zhu, Q. Liao, P.C. Sui, N. Djilali, J. Power Sources 195 (2010) 801–812.
- [23] J.-B. Dupont, D. Legendre, A.M. Morgante, J. Fuel Cell Sci. Technol. 8 (2011) 041008-1–041008-7.
- [24] N. Akhtar, P.J.A.M. Kerkhof, Int. J. Hydrogen Energy 36 (2011) 3076–3086.
- [25] C. Qin, D. Rensink, S.M. Hassanzadeh, S. Fell, J. Electrochem. Soc. 159 (4) (2012) B434–B443.
- [26] Y. Cai, T. Chen, T. Yang, J. Xiao, J. Power Sources 209 (2012) 90–104.
- [27] S.C. Cho, Y. Wang, K.S. Chen, J. Power Sources 206 (2012) 119–128.
- [28] S.C. Cho, Y. Wang, K.S. Chen, J. Power Sources 210 (2012) 191–197.
- [29] E.C. Kumbur, K.V. Sharp, M.M. Mench, J. Power Sources 161 (2006) 333–345.
- [30] C.D. Rath, S.G. Kandlikar, Colloids Surf., A: Physicochem. Eng. Asp. 384 (2011) 653–660.
- [31] P. Gopalan, S.G. Kandlikar, in: 3rd European Conference on Microfluidics (2012).
- [32] P. Gopalan, S.G. Kandlikar, J. Electrochem. Soc. 159 (8) (2012) F468–F475.
- [33] P. Gopalan, S.G. Kandlikar, J. Electrochem. Soc. 160 (6) (2013) F487–F495.
- [34] P.K. Das, A. Grippin, A. Kwong, A.Z. Weber, J. Electrochem. Soc. 159 (5) (2012) B489–B496.
- [35] T.C. Wu, N. Djilali, J. Power Sources 208 (2012) 248–256.
- [36] M. Koz, S.G. Kandlikar, ECS Trans. 50 (2) (2012) 183–196.
- [37] J.P. Owejan, J.J. Gagliardo, J.M. Sergi, S.G. Kandlikar, T.A. Trabold, Int. J. Hydrogen Energy 34 (2009) 3436–3444.
- [38] P.T. Tsilingiris, Energy Convers. Manage. 49 (2008) 1098–1110.
- [39] C.R. Wilke, Chem. Eng. Prog. 46 (2) (1950) 95–104.
- [40] M.M. Mench, Fuel Cell Engines, Wiley, USA, 2008.
- [41] E.N. Fuller, P.D. Schettler, J.C. Giddings, Ind. Eng. Chem. 58 (5) (1966) 19–27.
- [42] Z. Lu, S.G. Kandlikar, C. Rath, M. Grimm, W. Domigan, A.D. White, M. Hardbarger, J.P. Owejan, T.A. Trabold, Int. J. Hydrogen Energy 34 (2009) 3445–3456.
- [43] G. Minor, N. Djilali, D. Sinton, P. Oshkai, Fluid Dyn. Res. 41 (2009) 045506–045527.
- [44] V.V. Dharaiya, S.G. Kandlikar, J. Heat Transfer 134 (2) (2012) 020911-1–020911-10.
- [45] R.K. Shah, D.P. Sekulic, Fundamentals of Heat Exchanger Design, John Wiley & Sons, USA, 2003, p. 477.